



Driving the sodium-oxygen battery chemistry towards the efficient formation of discharge products: The importance of sodium superoxide quantification

Marina Enterría^{a,*}, Marine Reynaud^a, Juan Ignacio Paredes^b, Lidia Medinilla^a, Reza Younesi^c, Nagore Ortiz-Vitoriano^{a,d,*}

^a Centre for Cooperative Research on Alternative Energies (CIC energiGUNE), Basque Research and Technology Alliance (BRTA), Vitoria-Gasteiz 01510, Spain

^b Instituto de Ciencia y Tecnología del Carbono, INCAR-CSIC, C/Francisco Pintado Fe 26, Oviedo 33011, Spain

^c Ångström Advanced Battery Centre (ÅABC), Department of Chemistry-Ångström Laboratory, Uppsala University, Uppsala SE-75121, Sweden

^d Ikerbasque, Basque Foundation for Science, Bilbao 48013, Spain

ARTICLE INFO

Article history:

Received 22 September 2021

Revised 29 November 2021

Accepted 2 December 2021

Available online 16 December 2021

Keywords:

Na-O₂ batteries

Graphene

Transmission X-Ray diffraction

Rietveld refinement

Na-O₂ quantification

Parasitic chemistry

Cathode design

ABSTRACT

Sodium-oxygen batteries (SOBs) have the potential to provide energy densities higher than the state-of-the-art Li-ion batteries. However, controlling the formation of sodium superoxide (NaO₂) as the sole discharge product on the cathode side is crucial to achieve durable and efficient SOBs. In this work, the discharge efficiency of two graphene-based cathodes was evaluated and compared with that of a commercial gas diffusion layer. The discharge products formed at the surface of these cathodes in a glyme-based electrolyte were carefully studied using a range of characterization techniques. NaO₂ was detected as the main discharge product regardless of the specific cathode material while small amounts of Na₂O₂·2H₂O and carbonate-like side-products were detected by X-ray diffraction as well as by Raman and infrared spectroscopies. This work leverages the use of X-ray diffraction to determine the actual yield of NaO₂ which is usually overlooked in this type of batteries. Thus, the proper quantification of the superoxide formed on the cathode surface is widely underestimated; even though is crucial for determining the efficiency of the battery while eliminating the parasitic chemistry in SOBs. Here, we develop an ex-situ analysis method to determine the amount of NaO₂ generated upon discharge in SOBs by transmission X-ray diffraction and quantitative Rietveld analysis. This work unveils that the yield of NaO₂ depends on the depth of discharge where high capacities lead to very low discharge efficiency, regardless of the used cathode. We anticipate that the methodology developed herein will provide a convenient diagnosis tool in future efforts to optimize the performance of the different cell components in SOBs.

© 2021 Science Press and Dalian Institute of Chemical Physics, Chinese Academy of Sciences. Published by ELSEVIER B.V. and Science Press. This is an open access article under the CC BY-NC-ND license (<http://creativecommons.org/licenses/by-nc-nd/4.0/>).

1. Introduction

Although lithium-ion batteries (LiBs) are essential to today's portable electronic devices, they have almost reached their limits in terms of energy density (200–250 Wh kg⁻¹), cycle life (1000 cycles at >80% of capacity), and charge/discharge rate capabilities (1C) [1]. Aprotic sodium-oxygen batteries (SOBs) therefore arise as a possible alternative to LiBs due to their higher gravimetric energies (1108 Wh kg⁻¹ based on the NaO₂ discharge product) [2]. In SOBs, reactive oxygen species (ROS) are generated during discharge by an oxygen reduction reaction (ORR), which combine

with Na⁺ to form different sodium oxides at the surface of the “air-cathode”. Among these oxides, sodium superoxide (NaO₂), yielding nanometric and cubic-like morphology, is the commonly formed discharge product (Equation (1)). Upon charging, these oxides are dissolved back to the electrolyte to perform the oxidation of the oxygen anions (oxygen evolution reaction, OER) and Na is deposited at the anode (Eq. (2)).



Up to date, the sluggish kinetics of ORR and OER, as well as their hardly controllable evolution, leads to unreproducible and parasitic cell chemistries, which hinders the commercialization of this type of battery. As mentioned previously, in the absence of any sec-

* Corresponding authors.

E-mail addresses: menteria@cicenergigune.com (M. Enterría), nortiz@cicenergigune.com (N. Ortiz-Vitoriano).

ondary reactions or moisture, and using a carbonate-free electrolyte, the sodium superoxide (NaO_2) product is preferentially formed. Driving the cell chemistry towards the formation of NaO_2 is crucial for the development of efficient, rechargeable, and competitive batteries. Hence, unlike other oxides, this crystalline discharge product can be reversibly oxidized to molecular oxygen during charge and does not remain in the electrode surface forming an electronic insulating passivation film.

However, NaO_2 can eventually disproportionate into sodium peroxide (Na_2O_2 , Eq. (3)) under certain conditions [3–5]. Besides, the presence of water traces in the cell or the release of protons by decomposition of the organic solvent have been reported to lead to hydration of NaO_2 after disproportionation, thus giving the hydrated peroxide ($\text{Na}_2\text{O}_2 \cdot 2\text{H}_2\text{O}$, Eq. (4)) [4].



The specific conditions of NaO_2 , Na_2O_2 or $\text{Na}_2\text{O}_2 \cdot 2\text{H}_2\text{O}$ formation are still very controversial due to the poor reproducibility of the cell chemistry. For example, Ortiz-Vitoriano et al. observed that the formation of $\text{Na}_2\text{O}_2 \cdot 2\text{H}_2\text{O}$ is not ascribed to the presence of water in the cell environment but to the moisture from the air environment [6]. Zhao et al. [7] and Pinedo et al. [8] observed that sodium-oxygen cells with closed and static oxygen atmosphere yielded NaO_2 , whereas cells supplied with flowing oxygen (99.99% pure) tended to produce $\text{Na}_2\text{O}_2 \cdot 2\text{H}_2\text{O}$. Finally, Bi et al. [9] demonstrated that the cell chemistry largely relies on the cell set-up, where even a small portion of air leakage in the system might lead to the formation of $\text{Na}_2\text{O}_2 \cdot 2\text{H}_2\text{O}$. Hence, the lack of conclusive information about the discharge product chemistry in SOBs can be ascribed to the different gas environments, cell configurations and electrolytes (e.g., impurities). Overall, the formation of the hydrated peroxide ($\text{Na}_2\text{O}_2 \cdot 2\text{H}_2\text{O}$) seems to require values of relative humidity in the cell environment around 20%, while 60%–70% humidity is known to generate NaOH [10].

Besides sodium oxides, other products arising from different parasitic reactions are generally found in SOBs during battery cycling. The highly reactive superoxide anion (O_2^-) promotes the decomposition of the electrolyte (solvent and salt) [11] while the peroxide anion (O_2^{2-}) formed during ORR can corrode the cathode material [12]. Consequently, sodium formate (NaCO_2H), sodium acetate (NaCOOCH_3) or sodium carbonate (Na_2CO_3) can be formed during battery operation. Likewise, the decomposition of the conducting salt in the electrolyte can also release side-products such as NaF , phosphorous oxides or chlorates, depending on the salt used [13]. The main factors for the limiting cyclability of SOBs are therefore the passivation of the air-electrode by the deposition of such electrically insulating side-products (different from NaO_2) and the electrolyte decomposition, which limit the discharge capacity values and hinder the rechargeability of the battery [14,15].

Among the different factors which influence the cell chemistry, the utilization of a suitable cathode material, enabling both an efficient reduction of oxygen and a homogeneous deposition of NaO_2 , is of utmost importance. Carbon materials are largely used as electrodes in SOBs due to their low cost, high surface area, chemical stability, conductivity and intrinsic catalytic activity toward the ORR/OER [16–18]. Gas diffusion layers (GDLs) are by far the most commonly used cathodes in SOBs due to their superior properties for the gas and liquid electrolyte management (i.e., high gas diffusivity and controlled electrolyte wettability) [15,19–22]. Nevertheless, the limited performance of GDLs at high operating current densities boosted the search for novel air-cathodes, where graphene has proven to be a promising material [23–25]. The rational design of the cathode can mitigate parasitic reactions by enhancing

the oxygen diffusion and catalysing the formation/dissolution of NaO_2 . Thus, driving the chemistry towards the efficient formation of NaO_2 requires (1) the use of a suitable air-electrode enhancing the oxygen diffusion, electrode wettability and electron transport, (2) a suitable characterization of the different discharge products formed in the cell and (3) a reliable quantification of the NaO_2 product. The latter parameter is of particular significance, as an accurate identification of the side-products formed in the battery is not always possible. For instance, the lack of crystallinity of some compounds prevents their identification by X-ray diffraction (XRD), while transitions allowed in Raman may be forbidden in IR or vice-versa, or some side-products are formed in the gas phase, such as H_2 , CO_2 or H_2O [26]. As a result, some of these side-products are barely detectable or undetectable at all by one or even several characterization techniques. In contrast, NaO_2 presents large and high crystalline cubic products yielding strong XRD signals. Therefore, quantifying the NaO_2 formed at the surface of the air-electrode appears as a realistic way to estimate the extent of parasitic reactions occurring in SOBs.

In this work, the discharge efficiency of three different air cathodes (a commercial gas diffusion layer and two graphene aerogels) was evaluated by developing a reliable methodology to quantify the NaO_2 formed on each cell system at certain operating conditions through a combination of transmission XRD and Rietveld analysis [27].

The reactions promoted by these carbon-based cathodes were further studied using complementary techniques to characterize the different discharge products deposited on their surface, including scanning electron microscopy (SEM) as well as Raman and infrared spectroscopies. The methodology proposed in this work not only allows a quantification of the NaO_2 discharge product, which is key to develop SOBs with high efficiencies, but more generally introduces a reliable, simple and readily accessible method than can be applied to other systems where a crystalline discharge product is formed.

2. Experimental

2.1. Preparation of graphene aerogels and selection of a reference commercial cathode.

Graphene aerogels were prepared from two different aqueous suspensions: (1) commercial graphene oxide (Graphenea, 0.4 wt% solution) and (2) lab-prepared electrochemically exfoliated graphene. The latter was obtained following a recently reported method [28]. Briefly, graphite foil ($25 \times 35 \times 0.5 \text{ mm}^3$ from Mer-sen) was anodically exfoliated using a platinum foil ($25 \times 25 \times 0.025 \text{ mm}^3$ from Goodfellow) as a counter electrode (cathode) in aqueous 0.1 M adenosine 5'-monophosphate disodium salt (Sigma Aldrich, $\geq 99.0\%$ purity HPLC) as the electrolyte. The graphite and platinum foils were placed at a distance of 2 cm from each other, immersed in the electrolytic medium and connected to an Agilent 6614C DC power supply to apply a positive potential of 10 V to the graphite foil. The delaminated graphite product was then collected and sonicated for 3 h in the same electrolytic medium (J.P. Selecta Ultrasons system, frequency: 40 kHz, power: 22 W L^{-1}). The obtained suspension was subjected to high-speed centrifugation (20,000g, 20 min) to completely sediment the material, followed by re-dispersion of the sediment in pure deionized water by 10 min sonication. After this washing step, the dispersion was subjected to low-speed centrifugation (200g, 20 min) to separate poorly delaminated components (sediment) from the well exfoliated nanosheets retained in the supernatant. The concentration of the as-obtained electrochemically exfoliated graphene suspension (EEG), as well as the commercial graphene oxide suspension

(GO), was adjusted to 2 mg mL⁻¹, and then 40 mL of each dispersion were frozen by immersion in liquid N₂ (−176 °C). The frozen suspensions were subsequently freeze-dried in a Telstar LyoQuest apparatus for 72 h to obtain aerogel monoliths, which were compacted and punched into 0.95 cm² circular electrodes. While the aerogel prepared from EEG was used directly as a cathode (EEG; mass: 4.1 ± 0.4 mg), the one prepared from GO was thermally reduced to make it electrically conductive. To this end, the circular GO electrodes were heat-treated at 800 °C under an argon flow (flow rate: 80 mL min⁻¹; heating rate: 5 °C min⁻¹; dwell time: 1 h) to give reduced graphene aerogel cathodes (rGO; mass: 1.5 ± 0.3 mg). A commercial gas diffusion layer (QuinTech, Freudenberg H23C6), which is commonly used as an air-cathode in metal-air batteries, was used as a reference material and denoted as carbon paper (CP; mass: 15 ± 0.2 mg). This gas diffusion layer was also punched out to give electrodes of the same area as the graphene-based electrodes.

2.2. Physicochemical characterization of pristine electrodes and discharged cathodes

The porosity of the pristine air-electrodes was studied using an ASAP2020 adsorption analyser (Micromeritics). The N₂ adsorption-desorption isotherms were measured at −196 °C in the relative pressure range from 10⁻⁴ to 0.99. Samples were degassed at 200 °C for 16 h under vacuum. The specific surface area (*S*_{BET}) was calculated according to the Brunauer-Emmett-Teller (BET) method [29,30] from the nitrogen isotherms in the relative pressure range of 0.05–0.25. The morphology of the different materials was studied by scanning electron microscopy (SEM) using a FEI Quanta250 microscope operating at 20 kV. The chemical nature/structure of the pristine electrode materials and the discharge products were studied by complementary characterization techniques in order to detect both amorphous and crystalline compounds. To this end, Raman spectra were recorded with a Renishaw spectrometer (Nanonics Multiview 2000) by focusing with a 50× long working distance objective and operating with a laser excitation wavelength of 532 nm. The spectra were obtained by performing 10 acquisitions with 10 s of dwell time using a power beam of 1%. A silicon wafer was used for calibration of the equipment. Attenuated total reflection Fourier transform infrared (ATR-FTIR) spectroscopy was performed on a Perkin-Elmer Spectrum 400 DTGS apparatus. Prior to characterization, the as-discharged cathodes were washed with fresh 1,2-dimethoxyethane (DME) solvent to remove excess conducting salt. In addition, suitable air-tight holders or inert argon atmosphere were used to ensure the chemical integrity of the sensitive discharge products during analysis.

The following reference compounds were used for the assignment of peaks in the Raman and ATR-FTIR spectroscopy analysis: sodium hydroxide (NaOH, Fisher Scientific extra pure), sodium formate (HCOONa, Alfa Aesar 98%), sodium oxalate (Na₂C₂O₄, Sigma Aldrich ACS reagent ≥99.5%), sodium acetate (CH₃COONa, Sigma Aldrich anhydrous Reagent Plus ≥99%), sodium carbonate (Na₂CO₃, Scharlau anhydrous Reagent grade ACS 99.8%), sodium oxide (Na₂O, Sigma Aldrich 80%) sodium peroxide anhydrous (Na₂O₂, Alfa Aesar 95%) and potassium superoxide (KO₂, Acros Organics). All these compounds were stored in an Ar-filled, dry glove box (H₂O < 0.1 ppm).

2.3. Cell assembly and deep discharge galvanostatic measurements

Stainless steel, 2-electrode Swagelok®-type cells equipped with an O₂ reservoir were used for evaluating the deep discharge capacity of the different carbon-based cathodes. The electrolyte was prepared by drying DME solvent over molecular sieves (3 Å, Sigma

Aldrich) for one week and sodium hexafluorophosphate salt (NaPF₆, 99% Stella Chemifa) under vacuum at 120 °C for 24 h. Electrolyte solutions comprising 0.1 M NaPF₆ in DME were prepared in the glove box and their water content was determined with an 899 Karl Fisher Coulometer (Metrohm). All the electrolytes prepared in this work yielded amounts of water below 8 ppm. The Swagelok®-type sodium-oxygen cells were dried overnight and transferred to an Ar-filled glove box (H₂O < 0.1 ppm, O₂ < 0.1 ppm, Jacomex, France). Stainless steel mesh (Alfa Aesar, 45002 gauze) was used as the current collector for the air cathode, the 0.1 M NaPF₆ solution in DME as the electrolyte, Celgard® H2010 membrane as the separator and a sodium metal disc (0.95 cm², Panreac 99.8% purity) as both the reference and counter electrode. The assembled cells, which have a static O₂ gas reservoir, were pressurized with pure oxygen (99.99% pure) to ~1 atm and a resting period of 8 h at open circuit voltage (~2.2–2.3 V vs. Na⁺/Na) was set up. Galvanostatic discharge measurements were performed in a Biologic-SAS VMP3 potentiostat at a current density of 0.1 mA cm⁻² for four different limited capacities (0.5, 1, 1.5 and 2 mAh cm⁻²) or to deep-discharge setting a lower cut-off voltage of 1.8 V vs. Na⁺/Na.

2.4. Quantification of the NaO₂ discharged on the carbon-based cathodes

The amount of sodium superoxide deposited on the surface of the carbon-based cathodes was quantified from the X-ray diffraction (XRD) patterns for the different discharged cathodes as described in Section 2.3, stacked with an internal silicon reference. To this purpose, homogeneous silicon inks were prepared by ball milling 0.1 g of highly crystalline silicon powder (640b NIST, Fig. S1a) together with a polyvinylidene fluoride (PVDF) solution (5 wt% in N-methyl-2-pyrrolidone, NMP) in a 70:30 wt:wt% proportion. The mixture was cast onto a Solupor® paper using an automatic film coater, adjusting the thickness to 150 μm (Fig. S1b). The as-coated paper was dried at 45 °C for 20 h, punched into 16 mm circular objects and dried under a vacuum at 60 °C for 15 h in the glove box. The silicon mass loading on the dry circular paper references was 0.60 ± 0.03 mg. The different discharged cathodes were stacked onto these circular silicon references (Fig. S1c) and vacuum-sealed in polymer-coated thin Al foils (5x5 mm²) inside the glove box, as shown in Scheme 1. The XRD patterns of the as-prepared, air-tight envelopes were acquired in transmission configuration using a Stoe & Cie GmbH Stadi P X-ray powder diffractometer equipped with 1 K Dectris Mythen 1 K detector and Ge monochromator (Cu Kα1) operating at 45 kV and 40 mA. The XRD patterns were collected in a 2θ angle range from 25 to 60°, at a step size of 0.5° and with a total acquisition time of 110 min. The X-ray beam, which covered 31% of the surface of the discharged cathodes (beam size = 10 × 3 mm²), was focused towards the centre of the electrodes. The efficiency of the battery was calculated based, exclusively, on the formation of NaO₂ (parasitic products were not considered) using the following calculations.

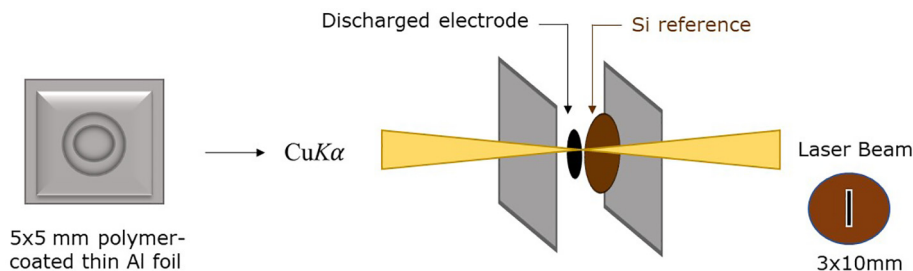
2.4.1. Calculation of the yield of NaO₂

The NaO₂ yield efficiency was calculated by the relation between (1) the theoretical amount of superoxide that must be formed for a given discharge capacity and (2) the actual amount which was detected experimentally by transmission XRD.

$$\text{Yield NaO}_2 = \frac{\text{Experimental amount of NaO}_2}{\text{Theoretical amount of NaO}_2} \times 100$$

2.4.2. Calculation of the theoretical amount of discharged NaO₂

The theoretical amount of NaO₂ formed as function of the depth of discharge was calculated by using the Faradaýs Law:



Scheme 1. Schematic representation of the sample preparation used for the quantification of NaO₂ by transmission XRD.

$$\rho_{\text{NaO}_2} = \frac{F \times Z_r}{M} = 487.5 \text{ AhKg}_{\text{NaO}_2}$$

where F is the Faraday constant (96,500 C mol⁻¹), Z_r is the number of electrons transferred in the reaction (1 electron in this case, dimensionless) and M is the molecular weight of NaO₂ (54.99×10^{-3} Kg_{NaO2} mol⁻¹).

The theoretical mass increase of NaO₂, as function of the depth of discharge, was calculated using the above-described theoretical amount as follows:

$$r_{\text{NaO}_2} = \frac{1}{\rho_{\text{NaO}_2}} = 2.05 \times 10^{-3} \text{ Kg}_{\text{NaO}_2} \text{ A}^{-1} \text{ h}^{-1} = 2.05 \text{ mg}_{\text{NaO}_2} \text{ mA}^{-1} \text{ h}^{-1}$$

As observed in Scheme 1, only the amount present on the area where the XRD beam hits the sample (i.e., 0.3 cm² area at the centre of the electrode) was considered for the calculation using the following formula:

$$\text{Theoretical amount of NaO}_2 = D_{\text{capacity}} \times r_{\text{NaO}_2} \times A_{\text{XRDbeam}}$$

where D_{capacity} is the discharge capacity in mAh cm⁻², r_{NaO_2} is the theoretical mass increase in mA⁻¹h⁻¹ and A_{XRDbeam} is the area of the XRD beam in cm².

For instance, for a discharge capacity of 2 mAh cm⁻², the theoretical amount of NaO₂ expected is 2 mAh cm⁻² × 2.05 mg mA⁻¹h⁻¹ × 0.3 cm² = 1.23 mg.

2.4.3. Calculation of the experimental amount of discharged NaO₂

All the XRD patterns were refined using Full Prof[®] Software, where Si (reference peak), NaO₂, Na₂O₂·2 H₂O and Al (bag/pouch cell-like holder) phases were identified by profile matching using Le Bail refinement. Si and NaO₂ phases were further refined in pseudo-Rietveld mode to extract their weight fraction (relative contribution to the patterns) and, thus, enabling a quantitative analysis for the latter phase. The experimental amount of NaO₂ discharged on each a cathode was calculated by the following formula:

$$\text{Experimental amount of NaO}_2 = \frac{\text{wt}\%(\text{Si}) \times \%R_{\text{WF}}(\text{NaO}_2)}{R_{\text{WF}}(\text{Si})}$$

where $R_{\text{WF}}(\text{Si})$ and $R_{\text{WF}}(\text{NaO}_2)$ are the relative weight fractions obtained by Rietveld refinement for Si and NaO₂, respectively. wt % (Si) is the weight in milligrams of silicon in a 0.3 cm² area (XRD beam area) of the prepared Solupor[®] paper/silicon patterns (Scheme 1). It is worth to mention that the application of this quantification method is linked to the cell design and, therefore, a prior study on the deposition behaviour for each specific cell design must be conducted (See Figs. S2 and S3 and their respective discussion).

3. Results and discussion

3.1. Characterization of the pristine carbon cathodes

The morphology of the different carbon-based cathodes was studied by SEM imaging. The commercial carbon paper (CP) is made of two stacked layers (Fig. S4): (1) a macroporous carbon fiber substrate (MPS) and (2) a microporous layer (MPL) comprised of a thin layer of carbon black, coated on the top of the MPS. The role of the MPS is to enhance the diffusion of O₂ molecules towards the electrolyte, while the MPL facilitates the electrical contact and the electrolyte diffusion, favours the ORR/OER reactions and accommodates the discharge products. Both layers are treated with polytetrafluoroethylene (PTFE) to modulate their wettability towards the electrolyte [21,22]. The discharge products formed in SOBs are mainly deposited on the MPL side of the commercial CP and, therefore, this is the side investigated in Fig. 1. The surface of the MPL layer presents a film morphology made up of nanometric particles and showing small cracks and holes (Fig. 1a). In contrast, the graphene-based aerogels exhibit a very rough surface derived from assembled graphene sheets with micrometer-sized pores/voids in between them. The GO-based aerogel (rGO) possesses large graphene sheets (25–50 μm, Fig. 1b) while its EEG counterpart (EEG) tend to have smaller sheets (10–20 μm, Fig. 1c).

The porous texture of the commercial CP and the graphene aerogels was studied by N₂ physisorption (Fig. 1d). Even though the graphene aerogels boast larger specific BET surface areas than that of the commercial CP (~100 vs 20 m² g⁻¹), the EEG cathode displays a larger total pore volume (0.45 cm³ g⁻¹) compared to rGO and CP (0.14–0.10 cm³ g⁻¹). The hysteresis loop together with the large increase in the amount of adsorbed N₂ observed at high relative pressures suggest that all the materials are highly mesoporous. The structural order of the studied cathode materials was evaluated by Raman spectroscopy (Fig. 1e). The Raman spectra of the three samples display the well-known D, G and 2D bands characteristic of carbon materials. A more defined and sharper 2D band at ~2700 cm⁻¹, together with narrower D and G bands, suggested a higher structural order in EEG [31]. The surface chemistry of the commercial CP and the graphene aerogels was also examined by ATR-FTIR spectroscopy. rGO yielded some C–O oxygen groups, while EEG and CP also exhibited C=O structures from carbonyl/-carboxyl functional groups. As expected from the PTFE treatment, some bands corresponding to C–F bonds are observed in the ATR-FTIR spectrum of CP. Furthermore, the presence of adenosine monophosphate molecules adsorbed on the surface of EEG [23] leads to the emergence of C=N and N=H bands in its spectrum.

3.2. Characterization of the discharged cathodes

The commercial carbon paper and the graphene aerogels were discharged to different depths using 0.1 M NaPF₆ in DME at a current density of 0.1 mA cm⁻¹ with a cut-off voltage of 1.8 V vs. Na⁺/

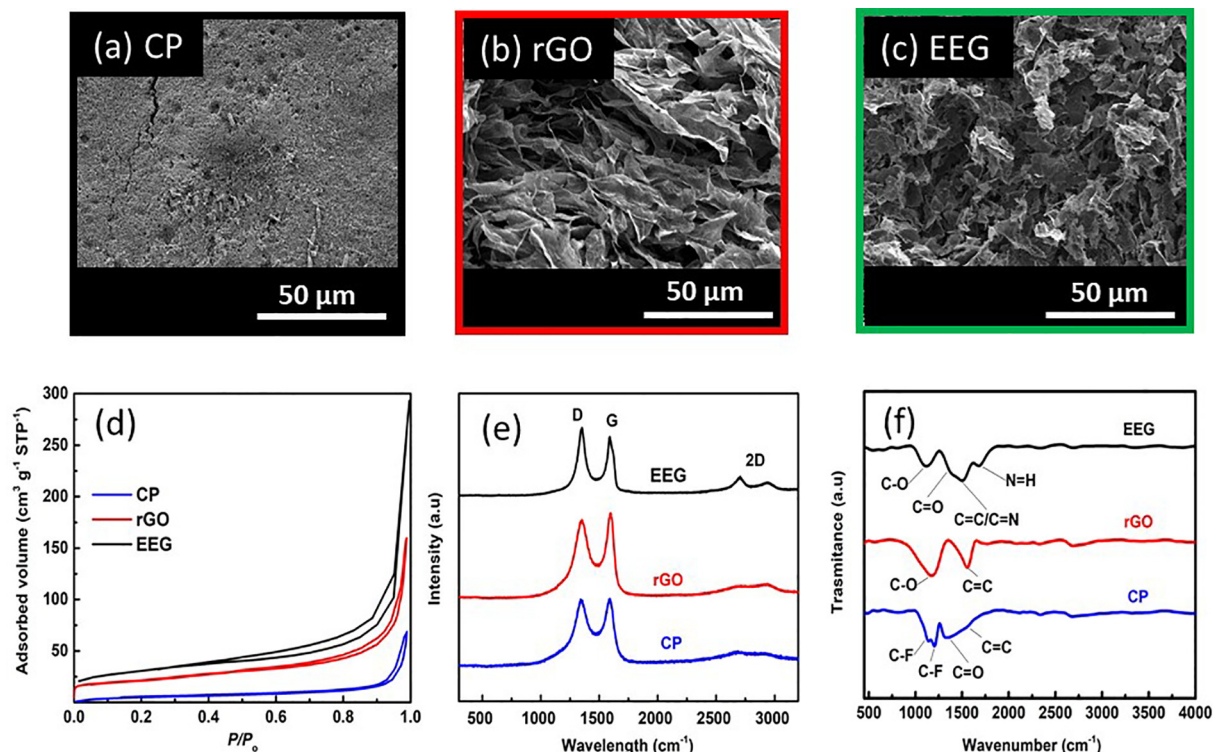


Fig. 1. SEM images of the (a) commercial CP and the prepared graphene aerogels; (b) rGO and (c) EEG. (d) Adsorption-desorption N_2 isotherms at $-176\text{ }^\circ\text{C}$, (e) Raman and (f) ATR-FTIR spectra of the three cathode materials.

Na. All cathodes discharged in Fig. 2 showed a discharge plateau between 2.08–2.11 V which corresponds to an overpotential of $\sim 175\text{ mV}$ (vs $E_{\text{Na}/\text{NaO}_2}^0 = 2.27\text{ V}$). Differences in the discharge voltage is a common challenge in Na- O_2 batteries; discharge experiments were therefore repeated several times and representative discharge curves for all the cathodes were selected and displayed in Fig. 2. Regarding deep discharge experiments, CP delivered a much larger capacity ($\sim 9.5\text{ mAh cm}^{-2}$) than those obtained for rGO ($\sim 3.4\text{ mAh cm}^{-2}$) and EEG ($\sim 4.3\text{ mAh cm}^{-2}$). The voltage noise observed while deep-discharging the EEG cathode was already observed in our previous work and was ascribed to the formation of electronically insulating side-products, mainly $\text{Na}_2\text{O}_2 \cdot 2\text{H}_2\text{O}$ [23].

The evolution of the morphology of the discharge products, as a function of the depth of discharge, was monitored by SEM imaging for all the studied cathodes (Fig. 3, Fig. S5). All the cathodes yielded cubic-shaped discharge products, which are associated to the for-

mation of NaO_2 . The cube size in CP and A-rGO cathodes remains stable at $\sim 5\text{--}12\text{ }\mu\text{m}$ regardless of the discharge depth. In contrast, the size of the cubes in A-EEG increases significantly as the discharge capacity increases from $3\text{ }\mu\text{m}$ for 0.5 mA cm^{-2} to $25\text{ }\mu\text{m}$ for full discharge. For the CP- and rGO-based cells, the most plausible mechanism is that oxygen is reduced at the surface of the air-electrode, diffuses to the electrolyte bulk and then NaO_2 nucleates/grows by a solution-mediated mechanism (Scheme 2), leading to a relatively homogeneous size distribution. Besides, the presence of defects in the rGO structure could also promote, to some extent, the deposition of the discharge products directly on the cathode surface (surface-mediated mechanism, Scheme 2). In the case of the EEG cathode, the nucleotide molecules adsorbed on the surface of the graphene nanosheets are believed to promote the nucleation of NaO_2 by a surface-mediated mechanism, leading initially to the formation of small-sized discharge products. As the

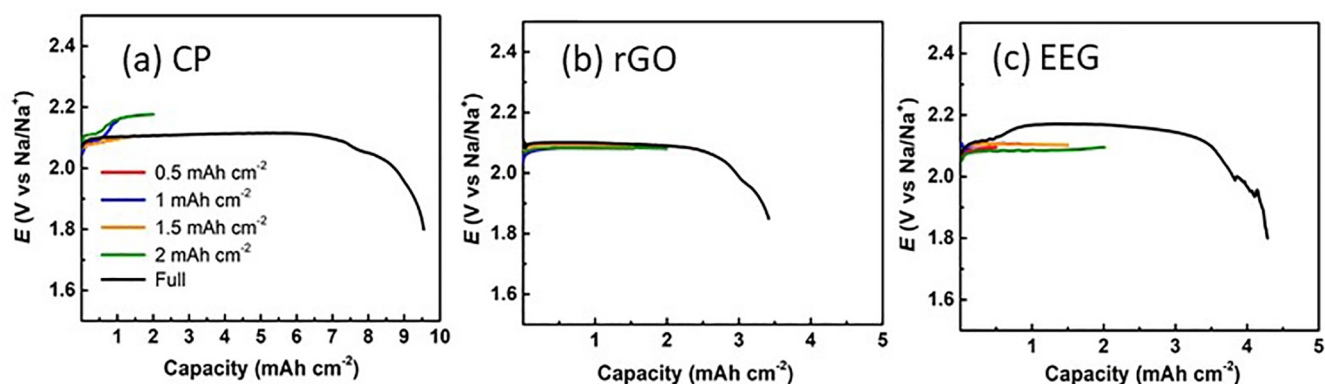


Fig. 2. Characteristic galvanostatic discharge profiles of the (a) commercial CP and (b) rGO and (c) EEG graphene aerogels, limited to either 0.5, 1, 1.5 or 2 mAh cm^{-2} , or discharged to full capacity.

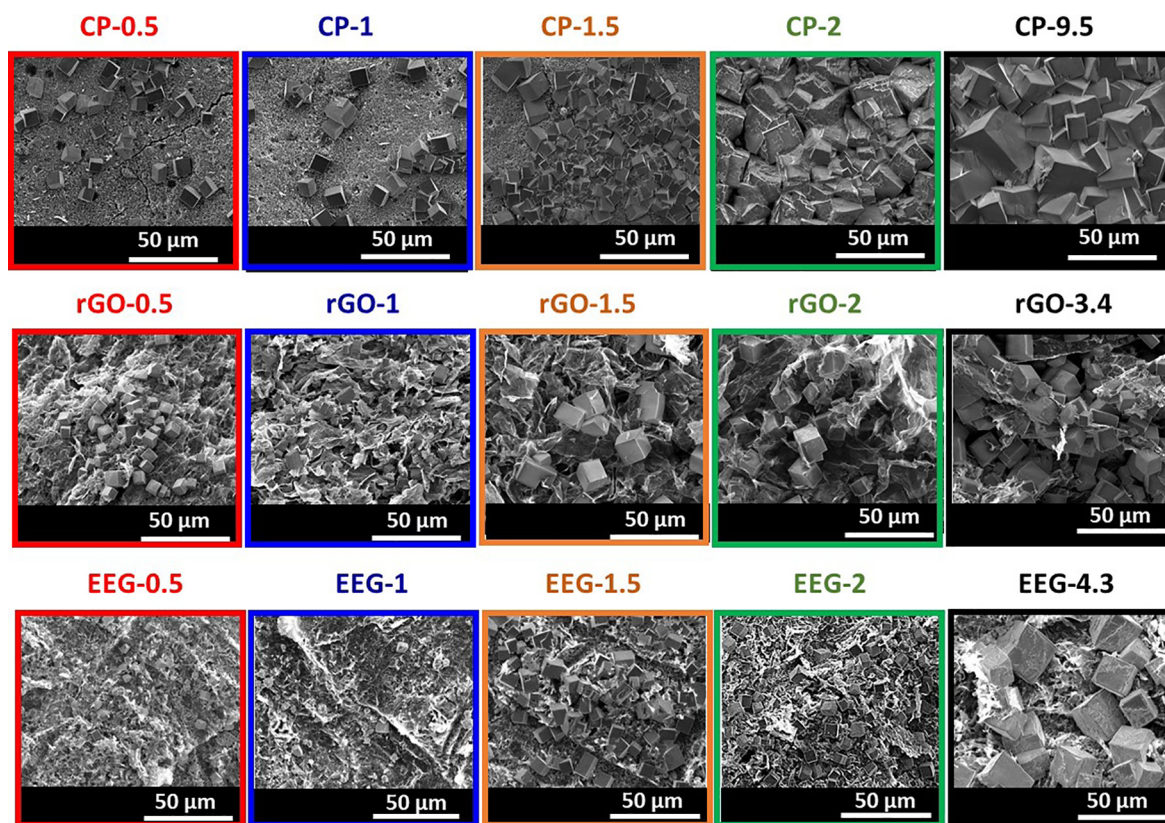


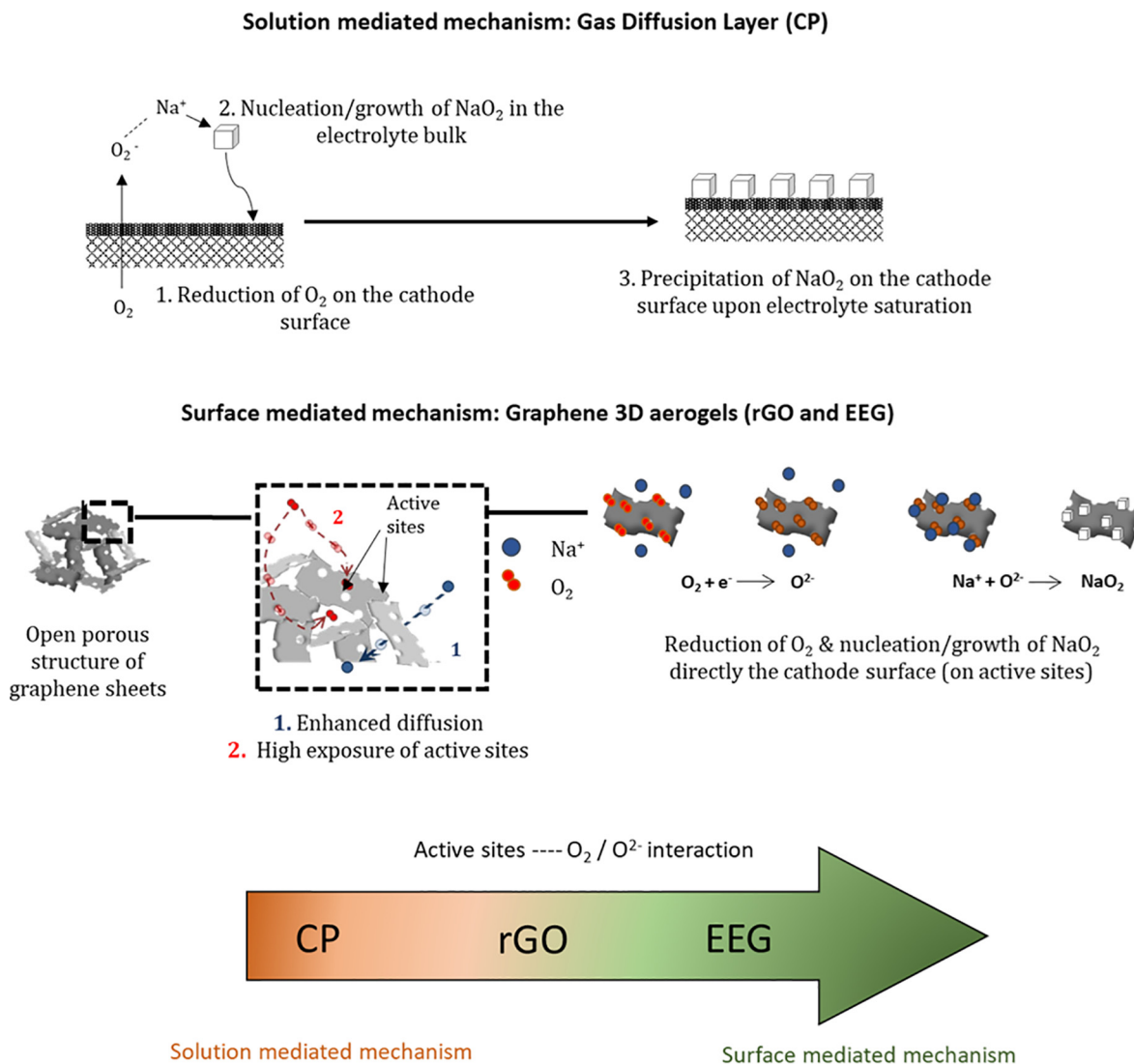
Fig. 3. SEM images at 2000X of the carbon-based cathodes (CP, rGO, EEG) discharged at different depths of discharge, as indicated by the number (referring to the capacity in mAh cm^{-2}) in the sample label.

discharge capacity increases, the nucleation sites on the EEG nanosheets could become saturated, so that the nucleation mechanism shifts to a solution-mediated, triggering the formation of much larger cubes. The combination of both mechanisms in this cathode might be responsible for such inhomogeneous size distribution along the cell discharge. An in-depth study on the discharge mechanism occurring in EEG cathodes can be found in [Scheme 2](#) and in our previous works [\[23,28\]](#). It is worth noting that precipitation of the discharge products on the surface of the CP cathode was much more extensive than that in the graphene-based aerogels for capacities above 1.5 mAh cm^{-2} . Thus, the discharge products in the latter aerogels seem to be more scattered among or in-between the graphene sheet bulk rather than in the top layers of the electrode.

Even though the cubic morphology is associated with NaO_2 formation, it has also been demonstrated that the surface layer of these cubes can be rich in other decomposition products in contact with an O-deficient region enclosing the bulk of the cubes [\[32,33\]](#). In order to detect the possible formation of other discharge products or side-products arising from superoxide/electrolyte decomposition, the discharged cathodes were characterized by XRD as well as Raman and ATR-FTIR spectroscopies. [Fig. 4](#) displays the evolution of the XRD patterns with the discharge capacity for the three different cathodes. The $38.2^\circ < 2\theta < 45^\circ$ region only contains reflections of the Al phase corresponding to the bag sample-holder (see [Scheme 1](#) and [Fig. S6](#)), but no relevant reflection ascribed to the different discharge products in SOB. This region is therefore not represented in [Fig. 4](#) for a better visualization of the phases of interest (i.e., NaO_2 and Si). The peaks corresponding to the silicon phase prepared in [Section 2.4](#) (located at $2\theta=28.45$, 47.32 and 56.15° , [Fig. S6](#)) are not discussed here, but will be used for the quantification of the NaO_2 discharge product in [Section 3.3](#).

Regardless of the depth of discharge, all the cathodes display the reflections corresponding to NaO_2 , in particular the (200) and (220) reflections at $2\theta \approx 32.6^\circ$ and 46.8° , respectively. The absence of other peaks related to sodium inorganic compounds suggest that NaO_2 is the main discharge product. As expected, the intensity of NaO_2 peaks increases with the depth of discharge for all the studied cathodes. Careful inspection of the XRD patterns shows a very weak peak at around $2\theta \approx 37.1^\circ$ that can be observed arising from the background of the patterns of some samples (see [Fig. S7](#)). This peak is usually attributed to the presence of $\text{Na}_2\text{O}_2 \cdot 2\text{H}_2\text{O}$ in the discharged samples [\[6,9,34\]](#) which, as previously noted, is generally formed upon decomposition of NaO_2 or by the presence of water traces in the environment, and can be indexed to the (230) plane of the orthorhombic cell proposed for this phase [\[35\]](#). Even though the emergence of this peak seemed to appear quite randomly, it was more frequently observed for the CP and EEG cathodes, especially for the latter ([Fig. S7](#)).

The detection limit of XRD might be lower than other characterization techniques and, in addition, this technique can only detect crystalline solids. In order to detect any amorphous products that can be deposited on the surface of either the cathodes or the NaO_2 cubes, the electrodes were also characterized by Raman and ATR-FTIR spectroscopies ([Fig. 5](#)). The assignment of the Raman peaks/infrared bands in the available literature is quite uncertain due to the lack of proper reference materials for NaO_2 and the difficult distinction between NaOH , Na_2CO_3 or Na_2O_2 and their hydrated forms [\[4\]](#). Consequently, we decided to record the corresponding spectra for some reference compounds that can form as possible discharge products in the SOB. In the case of NaO_2 , commercial potassium superoxide was used instead ([Fig. S8](#)). The assignment of peaks/bands was conducted on the basis of these reference patterns and the available literature [\[5,6,23,34,36–38\]](#).



Scheme 2. Different nucleation process proposed as function of the cathode used in this study.

Besides the Raman bands arising from the carbon-based cathodes (D, G and 2D bands in Fig. 1e), all the samples displayed an intense band at 1156 cm^{-1} , which corresponds to NaO_2 (Fig. 5a, c and e). Similar to XRD diffraction, NaO_2 is the main discharge product detected regardless of the cathode material or the depth of discharge. As an exception, the CP cathode discharged to full capacity (Fig. 5a) displays some low intensity peaks around $720\text{--}794\text{ cm}^{-1}$, which can be ascribed to the presence Na_2O_2 (Fig. S8). Also, a close inspection of the spectrum baseline by zooming into the $1100\text{--}1200\text{ cm}^{-1}$ region reveals a shoulder at $\sim 1136\text{ cm}^{-1}$ in the CP cathodes (Fig. S9), which suggests that the hydrated peroxide ($\text{Na}_2\text{O}_2 \cdot 2\text{H}_2\text{O}$) [6] is also formed on the surface of the discharged commercial carbon paper. Other discharge products, besides NaO_2 , Na_2O_2 or $\text{Na}_2\text{O}_2 \cdot 2\text{H}_2\text{O}$ are detected by studying the discharged cathodes by ATR-FTIR spectroscopy (Fig. 5b, d and f). The band centred at $830\text{--}840\text{ cm}^{-1}$ arises from $\text{C}=\text{O}$ bonding in carbonates, whereas those at $1420\text{--}1430\text{ cm}^{-1}$ and $1560\text{--}1580\text{ cm}^{-1}$ can be either ascribed to $\text{Na}_2\text{O}_2 \cdot 2\text{H}_2\text{O}$ or groups incorporating $\text{C}=\text{O}$ structures, such as carbonates, formates or acetates (see Fig. S8). CP (Fig. 5b) and A-EEG (Fig. 5f) cathodes also present some additional bands around $980\text{--}990\text{ cm}^{-1}$ and $\sim 1950\text{--}2450\text{ cm}^{-1}$ that are related to the formation of $\text{Na}_2\text{O}_2 \cdot 2\text{H}_2\text{O}$. No bands corresponding to NaO_2 are detected by this technique, as the homopolar nat-

ure of its O-O bonding hinders its identification by ATR-FTIR spectroscopy [38].

After characterization of the discharged cathodes by different analytical techniques, it can be concluded that NaO_2 is the major discharge product in a glyme-based electrolyte and well-sealed cell system. Nevertheless, a minimal contribution from other discharge products has been detected. The presence of Na_2O_2 or $\text{Na}_2\text{O}_2 \cdot 2\text{H}_2\text{O}$ seems to be negligible for the rGO cathodes, whereas the formation of these products in both CP and EEG cathodes is more noticeable, particularly for the latter. The highly hygroscopic character of the adenosine monophosphate molecules adsorbed on the surface of the EEG nanosheets could hinder the removal of trace water from the bulk of the electrode, even after vacuum drying at high temperatures [23]. Consequently, water traces remaining in the cathode could promote the decomposition of NaO_2 to $\text{Na}_2\text{O}_2 \cdot 2\text{H}_2\text{O}$. In the case of CP, the electron donating nature of the C-F bonding in the PTFE polymer might increase the stability of the $\text{O}_2^{\cdot -}$ anion in the electrolyte phase by expelling it from the cathode surface, favouring the nucleation, growth and further precipitation of peroxides upon saturation. Likewise, the degradation of PTFE polymer by the attack of oxygen radicals could release protons to the electrolyte [38], promoting the formation of $\text{Na}_2\text{O}_2 \cdot 2\text{H}_2\text{O}$. The formation of carbonates, acetates and formates is also acknowledged in

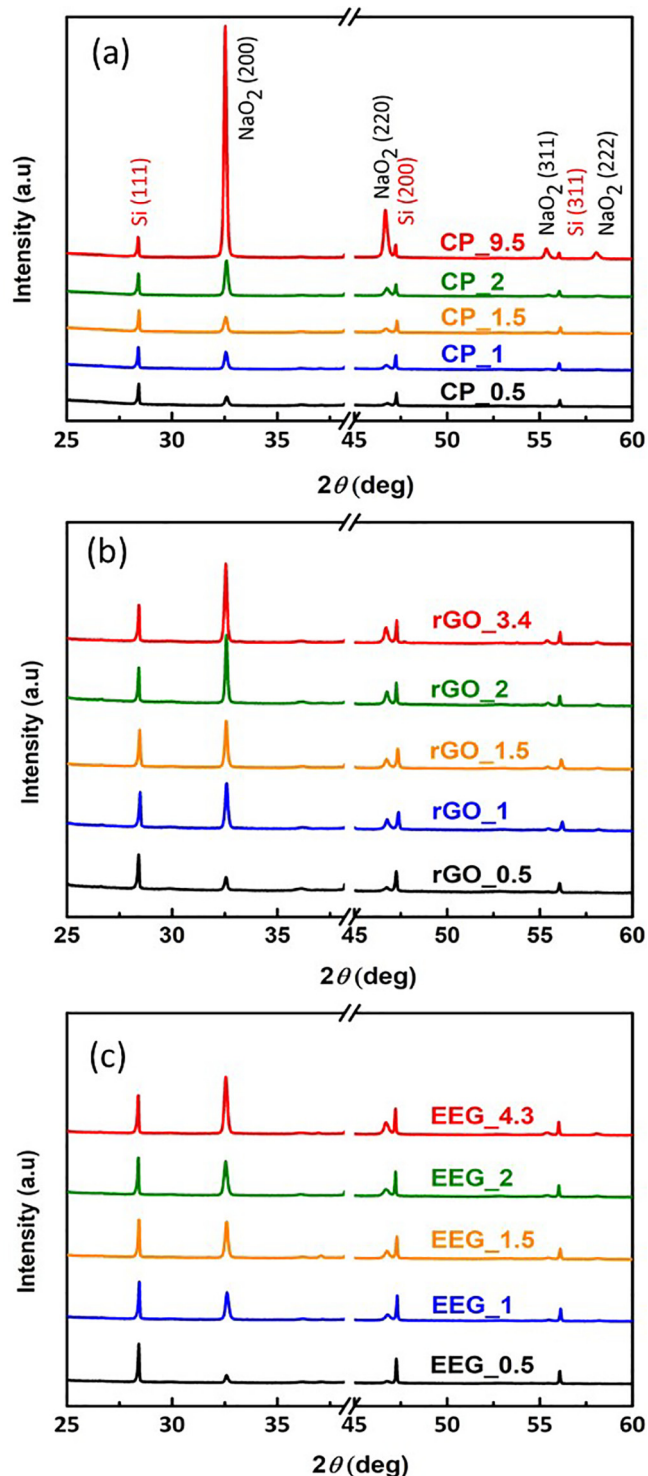


Fig. 4. XRD patterns for all the cathodes discharged in this study; (a) CP, (b) rGO and (c) EEG, at different depth of discharge as indicated in the sample label.

all the discharged cathodes, probably derived from the attack of O_2^- ion to electrolyte molecules or the corrosion of the carbon cathodes by the highly oxidative O_2^- peroxide anion.

3.3. Quantification of NaO_2 discharged on the surface of the carbon-based cathodes.

As previously discussed, the identification of side-products in SOBs is not always straightforward. In fact, although the type

and number of parasitic products identified in Section 3.2 seemed to be small, the total amount of NaO_2 is unknown, which has a great impact on the efficiency of the cells. The partially amorphous character of some side-products, together with their low quantity hinders their reliable identification and quantification by techniques such as XRD. Some of the discharge and side-products in SOBs, such as NaO_2 , Na_2O_2 , Na_2CO_3 and $NaOH$, have been unequivocally identified. In contrast, Na_2O_2 is a highly unstable compound which can exhibit either amorphous or crystalline phases, or even form different hydrates, so unequivocal identification of this compound is challenging. Besides, the lack of reliable crystallographic data for the dehydrated peroxide (the most common formed in SOBs) hinders an in-depth characterization of this phase using Rietveld refinement. The cell parameters for $Na_2O_2 \cdot 2H_2O$ have been scarcely reported [35] and its actual crystal structure is still unknown. Conveniently, the formation of an amorphous phase in NaO_2 is highly unlikely and the crystallographic data have been identified with absolute certainty [3,11,39–41].

Taking all this into consideration, quantifying the amount of NaO_2 by XRD is an interesting and reliable approach to evaluate the cell efficiency, opening an avenue for future studies that aim at avoiding the SOB parasitic chemistry. The amount of NaO_2 formed in all the discharged cathodes (Fig. 2) was quantified from the refinement of the XRD patterns presented in Fig. 4, using the nanocrystalline silicon as internal intensity reference (Scheme 1). The Rietveld refinement method [27] enables a quantitative phase analysis based on the fact that the ratio of the diffracted intensities varies linearly as a function of the weight fractions for the crystalline phases of a mixture. Here, nanocrystalline silicon films stacked with the discharged cathodes in the Al bag (Scheme 1) were used as an internal reference of known mass to determine the relative amount of the crystalline phases formed on the discharged cathodes by using the equations displayed in Section 2.4. The XRD patterns were refined using four different crystalline phases: Si, NaO_2 , Al and $Na_2O_2 \cdot 2H_2O$. The irregular background (due to the polymer coating of the Al foil, Fig. S6) was first extracted as a linear interpolation between points from the blank pattern of an empty Al bag. The Al and $Na_2O_2 \cdot 2H_2O$ phases were treated in LeBail mode [35,42] due to (1) the lack of crystallographic data for the latter and (2) the high preferential orientation observed for the Al signals of both layers of the Al bag. Conversely, the Si and NaO_2 phases were treated in pseudo-Rietveld mode, *i.e.*, taking into account their respective crystal structure for the peak intensity calculation but without refining the atomic positions, using the reported crystal structures [43,44] so as to extract their relative contribution to the XRD patterns (Table S1). Some examples of pattern refinement are presented in Figs. S10, S11 and S12, while the results of the quantitative analyses for all the samples are gathered in Table S1. As well, as an example, the crystallographic parameters obtained from the analysis of the CP_0.5 sample are shown in Table S2. The amount of NaO_2 deduced from the quantitative analysis of the XRD patterns is plotted in Fig. 6 (black solid circles) for the three carbon-based cathodes at different depths of discharge. The theoretical amount of NaO_2 , deduced from the different discharge capacities and calculated as described in the Section 2.4 [45], is also given in the same Fig. (red hollow circles). In general, the efficiency of NaO_2 formation decreases for capacities above 1 mAh cm^{-2} for both CP (Fig. 6a) and rGO (Fig. 6b) cathodes. In contrast, the efficiency of the EEG cathode material is higher at smaller depths of discharge ($\leq 2 \text{ mAh cm}^{-2}$, Fig. 6c). For a better comparison, the NaO_2 yield efficiency for the three carbon-based cathodes is represented in Fig. 6(d). Despite of the much larger discharge capacity of the CP cathode (Fig. 2), the efficiency of the graphene-based aerogels is generally higher, particularly for the EEG cathode. This result could be ascribed to a more extensive and superficial precipitation of NaO_2 in the CP

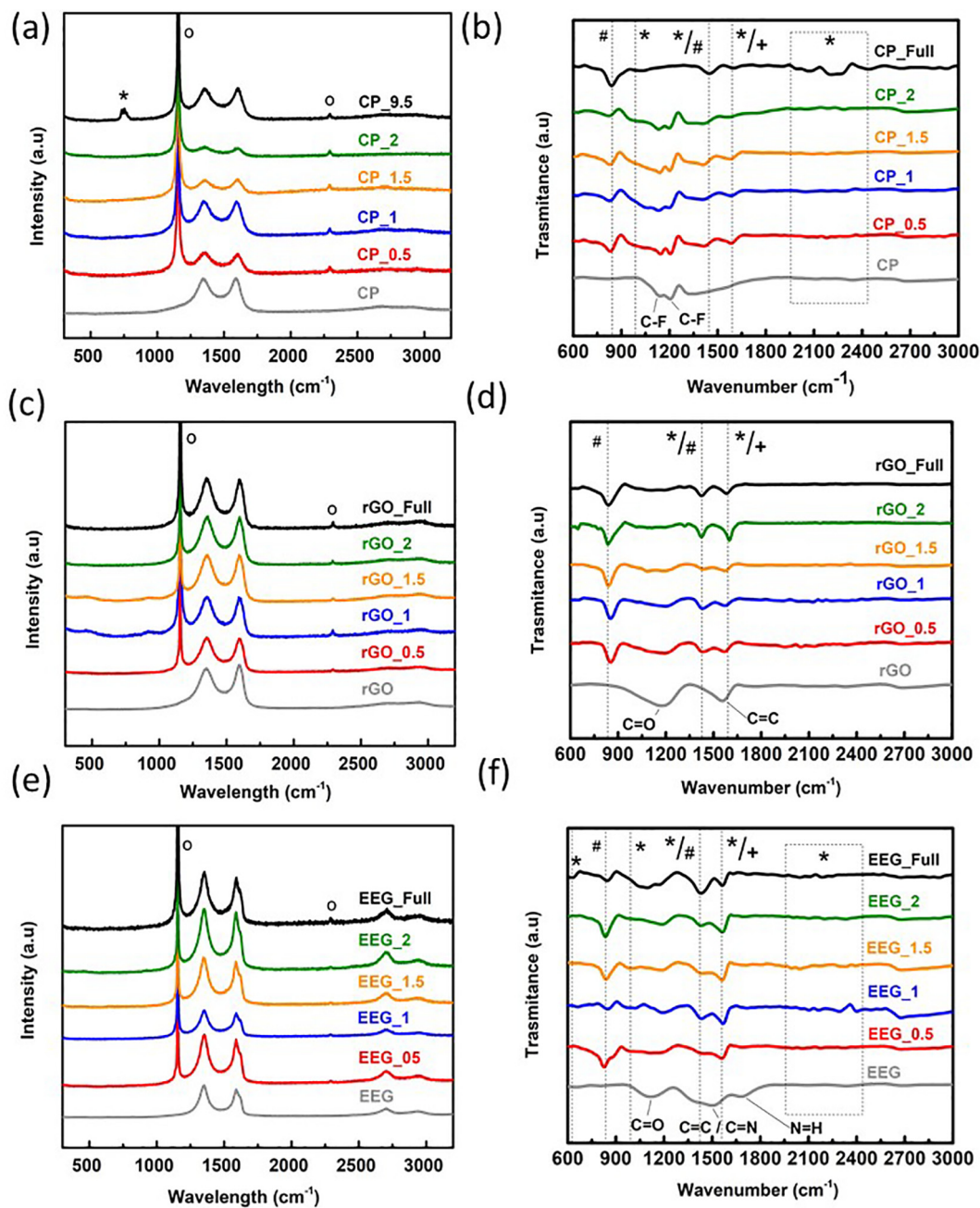


Fig. 5. Raman spectra for (a) CP, (c) A-rGO and (e) A-EEG, and FTIR spectra for (b) CP, (d) A-rGO and (f) A-EEG cathodes discharged at different depths of discharge. In grey, at the bottom of each figure, the spectrum of the pristine cathode materials is displayed (in grey) for comparison.

cathode as compared with graphene aerogels (Fig. 3), which could passivate (i.e., saturate) the available surface for the accommodation of further discharge products. Likewise, the commercial CP cathode presented the highest micropore surface area but the lowest porosity in terms of total pore volume (Fig. 1d). In contrast, the graphene-based aerogels displayed larger pore sizes (meso and macropores) and total pore volumes (Fig. 1d) which could promote a better dispersion of the discharge products with no apparent saturation of their surface (Fig. 3), suggesting a more accessible surface area. In this context, we have previously reported that the high total pore volume and presence of meso/macropores in the 3D open and accessible structure of the graphene aerogels

enhances the diffusion of both Na^+ and O_2 towards the inner structure of the cathodes [25]. Therefore, the active sites for the reduction of the O_2 gas are highly exposed enhancing the kinetics of the discharge reaction (Scheme 2).

On the other hand, two main mechanisms have been reported for the formation of NaO_2 discharge product: (1) the most common is the solution-mediated mechanism, where the discharge products nucleate and grow in the electrolyte bulk and then precipitate on the cathode surface upon saturation; and (2) the surface-mediated mechanism, where the discharge products nucleate directly at the surface of the cathode [3]. The CP cathode is more likely to perform a solution mediated mechanism. In the case of

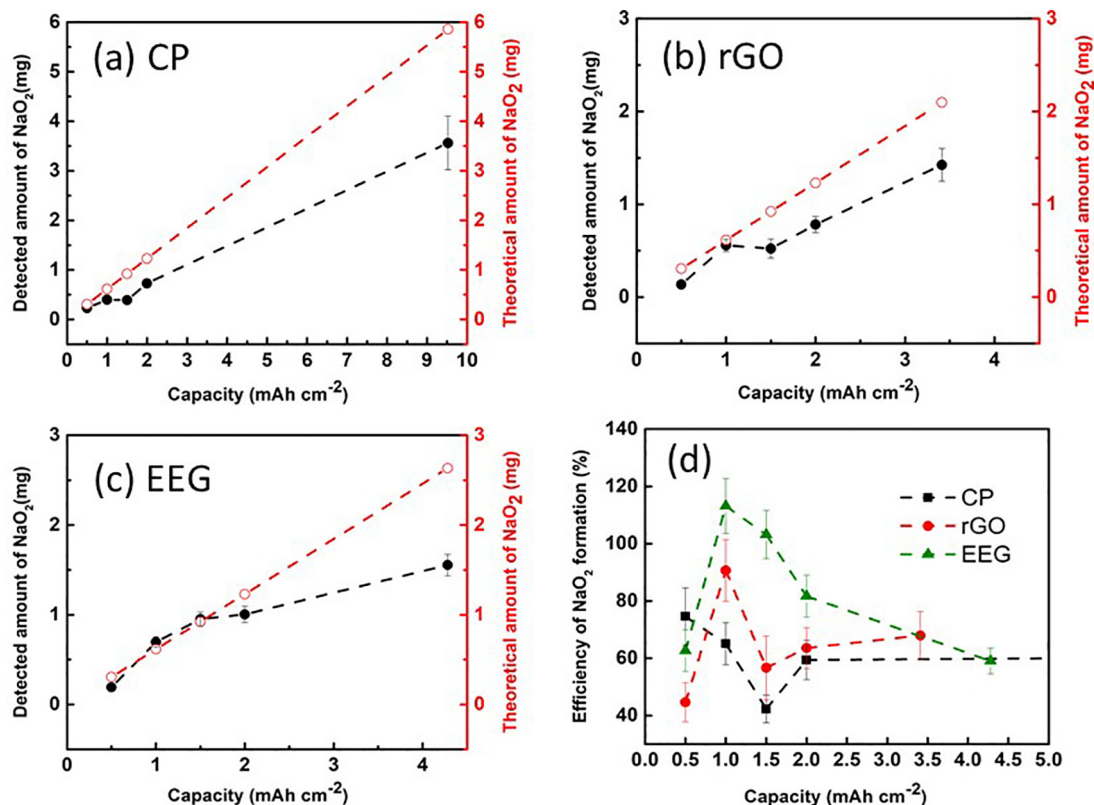


Fig. 6. Comparison of the theoretical amount of Na₂O₂ calculated from the discharged capacity (red hollow circles) and the experimental amount of formed Na₂O₂ as deduced from the quantitative analysis of the XRD patterns of the discharged electrodes (black solid circles) for (a) CP, (b) rGO and (c) EEG cathodes. (d) Efficiency of Na₂O₂ formation at different discharge depths relative to the theoretical yield for the three carbon-based cathodes.

the commercial gas diffusion layer (CP), the oxygen is reduced in the bulk of the electrode and the superoxide ion (O₂⁻) diffuses to the electrolyte solution to form the NaO₂ (Scheme 2). In contrast, rGO and EEG aerogels yield some catalytic sites in the surface of the graphene sheets which could promote the surface mediated mechanism to different extents (Scheme 2). The graphene sheets comprising the rGO aerogel present defects in the carbon lattice structure because of its preparation procedure (harsh oxidation of graphite and further thermal reduction). The existence of unpaired electrons located in such defects promotes the ORR reaction in very localized areas at the surface of the electrode [25], thus promoting the crystallization of NaO₂ by a surface-mediated mechanism (Scheme 2). The graphene sheets in EEG do not present as many structural defects as rGO (Fig. 1e) but the adenine nucleobase molecules adsorbed in its surface (see Experimental Section 2.1) can also catalyze the ORR. In this case, the surface-mediated mechanism is promoted by a cooperative effect arising from the nitrogen atoms and phosphate moieties present in the nucleotide. Thus, subsequently to the reduction of O₂ gas by the nitrogen atoms in the adenine nucleobase [46,47], the as-produced superoxide ions (O₂⁻) are trapped by the phosphates, also present in the same nucleotide molecule [23]. The immobilization of the reduced oxygen ions in the vicinity of the cathode will largely promote the formation of NaO₂ directly on its surface [28]. As illustrated in Scheme 2, the reaction mechanism in the studied cathodes is believed to change from solution to surface-mediated in the following order CP > rGO > EEG. For the graphene aerogel cathodes, rGO presents a combination of both mechanisms while EEG presents a stronger contribution of surface mediated route. In this regard, the higher efficiency of the EEG aerogel at lower depths of discharge can be ascribed to a combination of high electrical conductivity (low defect density in the graphene sheets),

high oxygen diffusion (open pore structure) and the presence of efficient catalytic active sites (adenosine monophosphate nucleotide) that promotes the nucleation of well-dispersed and small-sized NaO₂ cubes at the surface of the cathode. The solution-mediated mechanism generally leads to deposits of large cubic NaO₂ particles (~10 μm), while smaller cubes (~1–5 μm) or even film-like deposits are more related with the surface-mediated mechanism [23,28]. The 2.5–5 μm cubes observed in the EEG surface for capacities ≤2 mAh cm⁻² (Fig. 3 and S3) would be consistent with a better efficiency of this cathode at low-moderate discharge capacities (Fig. 6c). In contrast, the presence of larger cubes (~25 μm) for deep discharge experiments (Fig. 3 and S3), suggests the saturation of the catalytic sites at the surface of EEG cathode and, consequently, a change to solution-mediated mechanism. The change of the discharge mechanism when extending the discharge capacity to larger values could occur also in the case of the free-electron catalytic sites in rGO cathode but in a much lower extent. A predominant effect of solution mediated mechanism is proposed for CP and rGO cathodes and, therefore, a lower efficiency for low-moderate discharge capacities (Fig. 6c).

Regardless of the used cathode, the formation of NaO₂ (Fig. 6a, b and c) and therefore the discharge efficiency (Fig. 6d) drops substantially while deep discharging. As the battery discharge proceeds, the contribution of the parasitic reactions and the decomposition of the electrolyte by reactive oxygen species becomes significant. Hence, the massive deposition of electronically insulating products at deep discharge capacities leads to the passivation and pore clogging of the air-cathode material [45,48]. Consequently, further reduction of O₂ and deposition of NaO₂ is not favoured any longer, whatever the cathode used. In this context, avoiding such a sudden voltage drop while extending the flat discharge plateau (i.e., discharge capacity) as much as possible

is a great challenge for SOBs development. It can be therefore inferred that the parasitic reactions contribution is not so minimal for large discharge capacities. However, in this work, no significant contribution of such side-products was verified by a combination of XRD, Raman and ATR-FTIR spectroscopies. This might be explained by the fact that (1) the amount of these products is generally under the detection limit of the characterization techniques or (2) the formation of gaseous side-products through the battery operation has an important contribution in lowering the cell efficiency. The latter will be only detectable by techniques such as differential electrochemical mass spectrometry (DEMS) [12,26,49–51]. This technique, which detects the consumption/evolution of different gases during battery cycling, can be very useful to complement the here reported XRD-Rietveld analysis methodology. DEMS can monitor the consumption/evolution of O₂ gas during discharge and charge of the battery where, in an ideally operating cell, only oxygen evolves during charge. Also, this technique can detect the evolution of other gas-phase products during charge (CO₂, H₂O or H₂) which gives evidence for unwanted side reactions. On the other hand, DEMS is an “in-situ” (real-time) and quantitative diagnosis tool enabling an accurate monitoring of the battery efficiency but, unlike XRD, the nature of the discharge products cannot be directly identified. For this reason, both techniques are commonly coupled to get a complete and reliable estimation of the cell efficiency [50,51]. Whatever the case, the present work (1) validates a simple characterization method that could be used routinely in any laboratory having conventional XRD equipment and (2) provides a direct quantification of NaO₂ and, hence, the efficiency of the discharge in the SOB.

4. Conclusions

Three carbon-based cathodes (commercial gas diffusion layer and two-graphene based aerogels) have been discharged to different depths to study their discharge efficiency (amount of experimental NaO₂ formed vs theoretical) in sodium-oxygen batteries with the aim of relating it to the different reactions occurring in the cell. An “ex-situ” monitoring of the discharge products deposited on the cathode surface as a function of the discharge capacity revealed that (1) the main discharge product is NaO₂ regardless of the used cathode and (2) an apparent minimal contribution of Na₂O₂, Na₂O₂·2 H₂O and carbonate-like side-products is present. In accordance with literature, it was verified that using an airtight cell system with a static dry and pure oxygen reservoir and a glyme-based electrolyte, the parasitic chemistry seems to be negligible. Nevertheless, the quantification of the NaO₂ discharged in the different cathodes has shown that the discharge capacity is not maximized for any cell system or cathode used, except maybe at low discharge depths. It can be therefore concluded that the combination of different characterization techniques is not enough to identify the existing parasitic chemistry. In contrast, the quantification of NaO₂ can be a convenient and more trustworthy tool to evaluate the extent of the side reactions affecting the cell efficiency. Indeed, the present work proposes a straightforward ex-situ analysis method that determines the amount of NaO₂ in the sodium-oxygen cells by transmission X-ray diffraction and quantitative Rietveld analysis. As an example, the efficiency of graphene-based aerogels was compared with that of a commercial, carbon-based gas diffusion layer, which is widely employed as an air-electrode in metal-air batteries. Even though the commercial cathode displayed a higher capacity compared to that of the graphene-based aerogels, the efficiency of NaO₂ formation in the former appeared to be lower, especially for discharge capacities below ~2 mAh cm⁻². This result can be attributed to the faster saturation of the relatively compact commercial gas diffusion layer surface,

which is to be compared with the more open and higher surface area provided by the graphene-based aerogels. This information is of utmost importance to extend the capacities commonly used in cycling experiments. These capacities are normally limited to <1 mAh cm⁻² because of the lack of reversibility which might be due to the appearance of parasitic reactions at higher capacities. The NaO₂ quantification method discussed here can be extensively used as a first approach to select high performing cathode materials based on NaO₂ quantification.

This work provides a very simple and direct approach to estimate the efficiency of Na-O₂ batteries which could be extrapolated to other batteries/systems where crystalline products are formed. A more detailed knowledge of the processes that occur in the cells can only be achieved by in operando techniques which we will address in future studies, since it is not a trivial matter and will require a great deal of effort.

Declaration of Competing Interest

The authors declare that they have no known competing financial interests or personal relationships that could have appeared to influence the work reported in this paper.

Acknowledgments

M.E., L.M and N.O.-V. thank the European Union (Graphene Flagship-Core 3, Grant number 881603) for the financial support of this work. J.I.P. acknowledges funding by the Spanish Ministerio de Ciencia, Innovación y Universidades (MICINN), Agencia Estatal de Investigación (AEI) and the European Regional Development Fund (ERDF) through project RTI2018-100832-B-I00. R.Y. acknowledges financial support from StandUp for Energy and the Swedish Energy Agency. The authors also want to acknowledge the company GRAPHENEA for supplying the graphene oxide used in this work. The authors express special thanks to Dr. Yan Zhang for her help with Raman spectrometry measurements.

Appendix A. Supplementary data

Supplementary data to this article can be found online at <https://doi.org/10.1016/j.jechem.2021.12.014>.

References

- [1] A. Masias, J. Marcicki, W.A. Paxton, *ACS Energy Lett.* 6 (2021) 621–630.
- [2] S. Zhao, B. Qin, K.-Y. Chan, C.-Y.-V. Li, F. Li, *Batter. Supercaps* 2 (2019) 725–742.
- [3] H. Yadegari, X. Sun, *Trends Chem.* 2 (2020) 241–253.
- [4] C.L. Bender, D. Schröder, R. Pinedo, P. Adelhelm, J. Janek, *Angew. Chemie - Int. Ed.* 55 (2016) 4640–4649.
- [5] P. Adelhelm, P. Hartmann, C.L. Bender, M. Busche, C. Eufinger, J. Janek, *Beilstein J. Nanotechnol.* 6 (2015) 1016–1055.
- [6] N. Ortiz-Vitoriano, T.P. Batcho, D.G. Kwabi, B. Han, N. Pour, K.P.C. Yao, C.V. Thompson, Y. Shao-Horn, *J. Phys. Chem. Lett.* 6 (2015) 2636–2643.
- [7] N. Zhao, C. Li, X. Guo, *Phys. Chem. Chem. Phys.* 16 (2014) 15646–15652.
- [8] R. Pinedo, D.A. Weber, B. Bergner, D. Schröder, P. Adelhelm, J. Janek, *J. Phys. Chem. C* 120 (2016) 8472–8481.
- [9] X. Bi, R. Wang, L. Ma, D. Zhang, K. Amine, J. Lu, *Small Methods* 1 (2017) 1700102.
- [10] Q. Sun, H. Yadegari, M.N. Banis, J. Liu, B. Xiao, X. Li, C. Langford, R. Li, X. Sun, *J. Phys. Chem. C* 119 (2015) 13433–13441.
- [11] R. Black, A. Shyamsunder, P. Adeli, D. Kundu, G.K. Murphy, L.F. Nazar, *ChemSusChem* 9 (2016) 1795–1803.
- [12] B.D. McCloskey, A. Speidel, R. Scheffler, D.C. Miller, V. Viswanathan, J.S. Hummelshøj, J.K. Nørskov, A.C. Luntz, *J. Phys. Chem. Lett.* 3 (2012) 997–1001.
- [13] R. Younesi, G.M. Veith, P. Johansson, K. Edström, T. Vegge, *Energy Environ. Sci.* 8 (2015) 1905–1922.
- [14] P. Albertus, G. Girishkumar, B. McCloskey, R.S. Sánchez-Carrera, B. Kozinsky, J. Christensen, A.C. Luntz, *J. Electrochem. Soc.* 158 (2011) A343.
- [15] C. Wang, Y. Yu, J. Niu, Y. Liu, D. Bridges, X. Liu, J. Pooran, Y. Zhang, A. Hu, *Appl. Sci.* 9 (2019) 2787.
- [16] C.L. Bender, P. Hartmann, M. Vračar, P. Adelhelm, J. Janek, *Adv. Energy Mater.* 4 (2014) 1301863.

- [17] S. Liu, S. Liu, J. Luo, Carbon N. Y. 110 (2016) 518.
- [18] X. Lin, Q. Sun, K. Doyle Davis, R. Li, X. Sun, Carbon Energy 1 (2019) 141–164.
- [19] T.A. Ha, C. Pozo-Gonzalo, K. Nairn, D.R. MacFarlane, M. Forsyth, P.C. Howlett, Sci. Rep. 10 (2020) 1–10.
- [20] T. Danner, S. Eswara, V.P. Schulz, A. Latz, J. Power Sources 324 (2016) 646–656.
- [21] M. Chen, X. Jiang, H. Yang, P.K. Shen, J. Mater. Chem. A 3 (2015) 11874–11881.
- [22] F. Wang, X. Li, ACS Omega 3 (2018) 6006–6012.
- [23] M. Enterría, J.L. Gómez-Urbano, J.M. Munuera, S. Villar-Rodil, D. Carriazo, J.I. Paredes, N. Ortiz-Vitoriano, Small 17 (2021) 2005034.
- [24] X. Lin, J. Wang, X. Gao, S. Wang, Q. Sun, J. Luo, C. Zhao, Y. Zhao, X. Yang, C. Wang, R. Li, X. Sun, Chem. Mater. 32 (2020) 3018–3027.
- [25] M. Enterría, C. Botas, J.L. Gómez-Urbano, B. Acebedo, J.M. López Del Amo, D. Carriazo, T. Rojo, N. Ortiz-Vitoriano, J. Mater. Chem. A 6 (2018) 20778–20787.
- [26] N. Tsiouvaras, S. Meini, I. Buchberger, H.A. Gasteiger, J. Electrochem. Soc. 160 (2013) A471–A477.
- [27] H.M. Rietveld, J. Appl. Crystallogr. 2 (1969) 65–71.
- [28] J.M. Munuera, J.I. Paredes, M. Enterría, S. Villar-Rodil, A.G. Kelly, Y. Nalawade, J. N. Coleman, T. Rojo, N. Ortiz-Vitoriano, A. Martínez-Alonso, J.M.D. Tascón, ACS Appl. Mater. Interfaces 12 (2020) 494–506.
- [29] F. Rouquerol, J. Rouquerol, K.W.S. Sing, Adsorption by Powders & Porous Solids, Methodology and Applications, Academic Press, New York, Principles, 1999.
- [30] F. Rouquerol, Adsorption by Powders and Porous Solids : Principles, Academic Press, Methodology and Applications, 2013.
- [31] R. Rozada, J.I. Paredes, S. Villar-Rodil, A. Martínez-Alonso, J.M.D. Tascón, Nano Res. 6 (2013) 216–233.
- [32] I. Landa-Medrano, A. Sorrentino, L. Stievano, I. Ruiz de Larramendi, E. Pereiro, L. Lezama, T. Rojo, D. Tonti, Nano Energy 37 (2017) 224–231.
- [33] Q. Sun, J. Liu, B. Xiao, B. Wang, M. Banis, H. Yadegari, K.R. Adair, R. Li, X. Sun, Adv. Funct. Mater. 29 (2019) 1808332.
- [34] H. Yadegari, Y. Li, M.N. Banis, X. Li, B. Wang, Q. Sun, R. Li, T.K. Sham, X. Cui, X. Sun, Energy Environ. Sci. 7 (2014) 3747–3757.
- [35] G.S. Hill, D.G. Holah, S.D. Kinrade, V.R. Magnuson, V. Polyakov, T.A. Sloan, Can. J. Chem. 75 (1997) 46–51.
- [36] Q. Sun, Y. Yang, Z.W. Fu, Electrochem. Commun. 16 (2012) 22–25.
- [37] J. Kim, H. Park, B. Lee, W.M. Seong, H.D. Lim, Y. Bae, H. Kim, W.K. Kim, K.H. Ryu, K. Kang, Nat. Commun. 7 (2016) 1–9.
- [38] J.P. Vivek, N.G. Berry, J. Zou, R.J. Nichols, L.J. Hardwick, J. Phys. Chem. C 121 (2017) 19657–19667.
- [39] P. Hartmann, C.L. Bender, M. Vračar, A.K. Dürr, A. Garsuch, J. Janek, P. Adelhelm, Nat. Mater. 12 (2013) 228–232.
- [40] N. Deng, G. Yang, W. Wang, Y. Qiu, RSC Adv. 6 (2016) 67910–67915.
- [41] A.L. Smith, C. Guéneau, J.L. Flèche, S. Chatain, O. Beneš, R.J.M. Konings, J. Chem. Thermodyn. 114 (2017) 93–115.
- [42] A.S. Cooper, Acta Crystallogr. 15 (1962) 578–582.
- [43] P. Ziegler, M. Rosenfeld, W. Kaenzig, Fischer Helv. Phys. Acta 49 (1976) 57–90.
- [44] D.M. Többsen, N. Stüßler, K. Knorr, H.M. Mayer, G. Lampert, Mater. Sci. Forum 378–381 (2001) 288–293.
- [45] C. Liu, M. Carboni, W.R. Brant, R. Pan, J. Hedman, J. Zhu, T. Gustafsson, R. Younesi, ACS Appl. Mater. Interfaces 10 (2018) 13534–13541.
- [46] Y. Xu, C. Chen, M. Zhou, G. Fu, Y. Zhao, Y. Chen, RSC Adv. 7 (2017) 26722–26728.
- [47] A. Kormányos, M.S. Hossain, F.W. Foss, C. Janáky, K. Rajeshwar, Catal. Sci. Technol. 6 (2016) 8441–8448.
- [48] L. Lutz, W. Yin, A. Grimaud, D. Alves Dalla Corte, M. Tang, L. Johnson, E. Azaceta, V. Sarou-Kanian, A.J. Naylor, S. Hamad, J.A. Anta, E. Salager, R. Tena-Zaera, P.G. Bruce, J.M. Tarascon, J. Phys. Chem. C 120 (2016) 20068–20076.
- [49] P. Hartmann, C.L. Bender, J. Sann, A.K. Dürr, M. Jansen, J. Janek, P. Adelhelm, Phys. Chem. Chem. Phys. 15 (2013) 11661–11672.
- [50] B. Sun, K. Kretschmer, X. Xie, P. Munroe, Z. Peng, G. Wang, Adv. Mater. 29 (2017).
- [51] X. Bi, R. Wang, Y. Yuan, Y. Yuan, D. Zhang, T. Zhang, L. Ma, T. Wu, R. Shahbazian-Yassar, K. Amine, K. Amine, J. Lu, Nano Lett. 20 (2020) 4681–4686.